Use of X-Ray Diffraction, Molecular Simulations, and Spectroscopy to Determine the Molecular Packing in a Polymer-Fullerene Bimolecular Crystal

*Nichole Cates Miller, Eunkyung Cho, Matthias J. N. Junk, Roman Gysel, Chad Risko, Dongwook Kim, Sean Sweetnam, Chad E. Miller, Lee J. Richter, R. Joseph Kline, Martin Heeney, Iain McCulloch, Aram Amassian, Daniel Acevedo-Feliz, Christopher Knox, Michael Ryan Hansen, Dmytro Dudenko, Bradley F. Chmelka, Michael F. Toney, Jean-Luc Brédas, and Michael D. McGehee**

Bulk-heterojunction (BHJ) solar cells made from blends of semiconducting polymers and fullerenes are attractive because they can be printed at low cost and have demonstrated efficiencies greater than 8%.[1–5] For these solar cells to produce current, excitons created during light absorption must reach a conjugated polymer (donor): fullerene (acceptor) interface and dissociate by charge transfer. Electrons and holes must then travel through the fullerenes and polymer, respectively, to reach the electrodes before recombination occurs. The forward and back charge-transfer processes and charge transport depend critically on the molecular packing. Slightly modifying the distance between the donor and acceptor can change the charge-transfer rates by more than an order of magnitude and consequently have an enormous impact on exciton dissociation and recombination.[6] Likewise, small changes in the molecular packing can significantly change charge-carrier mobilities.[7,8] Although important processes, such as charge separation and recombination, can depend on the polymer-fullerene wavefunction overlap, very little is known about how polymers and fullerenes pack on the molecular level since it is very difficult to accurately characterize molecular packing in BHJs.[9]

To design materials for BHJs rationally, it is therefore critical to develop an understanding of the molecular packing and its effects on key electronic processes. Until now, it has not been possible to establish the detailed molecular organization of BHJ blends using X-ray diffraction (XRD), because the blends were either amorphous or too disordered to yield enough XRD reflections to accurately determine the unit cell and molecular packing. The best BHJ material combinations have largely been discovered by trial and error. Currently no one is able to accurately predict why certain material combinations perform dramatically better than others or why certain processing conditions can improve performance in some materials combinations, yet reduce performance in others.

N. C. Miller,[†] Dr. R. Gysel, S. Sweetnam,
Dr. C. E. Miller, Prof. M. D. McGehee
Department of Materials Science and Engineering
Stanford University
Stanford, CA 94305, USA
E-mail: mmcgehee@stanford.edu

E. Cho,[†] Dr. C. Risko, Dr. D. Kim, Prof. J. L. Brédas
School of Chemistry and Biochemistry
Georgia Institute of Technology
Atlanta, GA 30332, USA

E. Cho[†]
School of Materials Science and Engineering
Georgia Institute of Technology
Atlanta, GA 30332, USA

Dr. M. J. N. Junk,[†] Prof. B. F. Chmelka
Department of Chemical Engineering
University of California
Santa Barbara, Santa Barbara, CA 93106, USA

Dr. C. E. Miller, Dr. M. F. Toney
Stanford Synchrotron Radiation Lightsource,
SLAC National Accelerator Laboratory
Menlo Park, CA 94025, USA

Dr. L. J. Richter, Dr. R. J. Kline
National Institute of Standards and Technology
Gaithersburg, MD 20899, USA

Prof. M. Heeney, Prof. I. McCulloch
Department of Chemistry
Imperial College London
London SW7 2AZ, UK

Prof. A. Amassian
King Abdullah University of Science and Technology (KAUST)
Physical Sciences and Engineering Division
Thuwal 23955-6900, Saudi Arabia

Dr. D. Acevedo-Feliz, Dr. C. Knox
King Abdullah University of Science and Technology (KAUST)
Visualization Core Laboratory
Thuwal 23955-6900, Saudi Arabia

Dr. M. R. Hansen, Dr. D. Dudenko
Max Planck Institute for Polymer Research
Ackermannweg 10, 55128 Mainz, Germany

[†] These authors contributed equally to this work.

DOI: 10.1002/adma.201202293

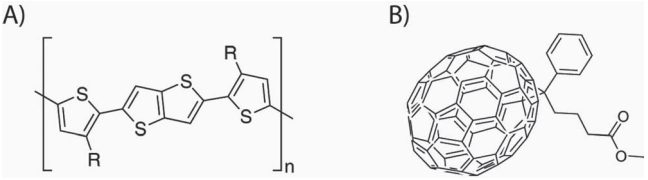

Figure 1. The chemical structures of PBTTT (A) and $PC_{71}BM$ (B). R can be $C_{12}H_{25}$, $C_{14}H_{29}$, or $C_{16}H_{33}$.

Here, we determine for the first time the detailed structure of a BHJ blend that establishes at the molecular level the properties and function of BHJ solar cells. Specifically, we use a combination of XRD techniques, molecular mechanics (MM) and molecular dynamics (MD) simulations, 2D solid-state NMR spectroscopy, and IR spectroscopy to determine the unit cell and atomic positions of the poly-(2,5-bis(3-alkylthiophen-2-yl)thieno[3,2-b]thiophene) (PBTTT):phenyl-C_{71}-butyric acid methyl ester ($PC_{71}BM$) bimolecular crystal, in which the $PC_{71}BM$ molecules intercalate between the PBTTT side chains (see **Figure 1** for molecular structures).[10] We find that the interactions between PBTTT and $PC_{71}BM$ are strong enough to severely disrupt the PBTTT packing by inducing bends and twists in the PBTTT backbone, as well as bends in the side chains, all of which allow increased interaction between the PBTTT and the $PC_{71}BM$. This finding: i) has significant implications for other polymer:fullerene blends, because strong polymer-fullerene interactions can cause polymer-fullerene intermixing in both semi-crystalline and amorphous blends; and ii) is surprising considering that until recently BHJs were thought to contain phase separated regions of relatively pure polymer and pure fullerene with very little mixing at the molecular scale.[11–14] Our work lends insight into the local packing in other blends with fullerenes present in the amorphous regions of semi-crystalline polymers. The methodology presented here makes it possible to determine the details of how polymers and fullerenes are arranged relative to each other.

We recently generated a phase diagram for PBTTT-C14:$PC_{71}BM$ blends[15] and demonstrated that the highest-efficiency PBTTT-C14:$PC_{71}BM$ solar cells contain 80 wt% $PC_{71}BM$.[16,17] At this composition, approximately half of the film consists of PBTTT-C14:$PC_{71}BM$ bimolecular crystals in which long-distance hole transport occurs and the other half consists of regions of fullerene that allow long-range electron transport. As the $PC_{71}BM$ fraction of the film decreases from 80 to 50 wt%, the power conversion efficiency drops from 2.35 to 0.16% due to the elimination of percolating fullerene clusters that are needed to provide electrons with adequately fast pathways to the electrodes.

PBTTT:$PC_{71}BM$ bimolecular crystals form upon spin-coating blends of PBTTT and $PC_{71}BM$ from a variety of solvents, as well as upon thermal annealing or solvent annealing of PBTTT:$PC_{71}BM$ bilayer films (Supporting Information, Figure S1). The structure of these bimolecular crystals appears to be independent of the solvent and processing conditions as long as a brief anneal is provided to allow the crystals to approach thermodynamic equilibrium. Diffraction from both the PBTTT-C14:$PC_{71}BM$ bimolecular crystal and pure PBTTT-C14 is observed in blends with 30 and 40 mol% $PC_{71}BM$, indicating that these blends contain excess polymer (**Figure 2** A). Blends with 60 mol% $PC_{71}BM$ exhibit diffraction from the bimolecular crystal and pure $PC_{71}BM$, indicating that these blends have excess $PC_{71}BM$. Diffraction from only the bimolecular crystal is observed in blends with exactly 50 mol% $PC_{71}BM$ (≈60 wt% $PC_{71}BM$), which corresponds to one $PC_{71}BM$ molecule per PBTTT-C14 monomer. The purpose of this study is to determine the detailed molecular structure of the PBTTT-C14:$PC_{71}BM$ bimolecular crystal. Consequently, all of the experiments described in the remainder of this manuscript were performed on films with 50 mol% $PC_{71}BM$ so that the pure bimolecular crystal could be studied. Although these films do not make efficient solar cells, the structural insights obtained are directly related to key molecular interactions and processes that govern macroscopic photovoltaic performance.

Figure 2B shows the experimental 2D grazing incidence X-ray scattering (2D GIXS) pattern for the PBTTT-C14:$PC_{71}BM$ bimolecular crystal. The intense (h00) reflections along the nominally q_z direction demonstrate the formation of a lamellar structure with the side chains oriented out of the plane of the substrate. As typically found for spin-cast films, the film is isotropic in the substrate plane, making it difficult to distinguish between (0k0), (00l) and (0kl) reflections, which all occur near the q_{xy} axis. Hence, two sets of unit-cell parameters are compatible with the limited number of experimentally available reflections. Both the orthorhombic lattice parameters a = 31 Å, b = 12.8 Å, and c = 13.5 Å and the monoclinic unit-cell parameters a = 31 Å, b = 10 Å, c = 13.5 Å, and α = 108° index all of the observed GIXS reflections. To distinguish between (0kl) reflections and identify the correct unit-cell parameters, we prepared a bimolecular-crystal film with preferred crystallographic orientation parallel to the substrate by aligning pure PBTTT-C14 using a flow-coating method,[18] spin-coating a $PC_{71}BM$ layer on top of the aligned PBTTT-C14 film using the orthogonal solvent dichloromethane, and annealing the resulting film to allow diffusion between the layers and the formation of aligned bimolecular crystals (Supporting Information, Figure S1). The in-plane angular dependence of the reflection intensities of the aligned film at q_{xy} = 0.49 Å^{-1} and q_{xy} = 0.66 Å^{-1} shows that the correct unit cell is monoclinic, rather than orthorhombic (Supporting Information, Figure S2,S3).

Solid-state NMR spectroscopy is sensitive to local compositional, structural, and dynamical environments, in both ordered and disordered regions of the materials.[19,20] Solid-state NMR spectroscopy therefore provides complementary insight on the molecular structures of PBTTT:fullerene blends,[21] including disordered moieties for which XRD is less useful. In particular, the solid-state 2D $^{13}C\{^1H\}$ heteronuclear correlation (HETCOR) NMR spectroscopy technique provides detailed information about the molecular interactions between PBTTT-C16 and $PC_{71}BM$ by identifying dipole–dipole-coupled ^{13}C and ^1H nuclei that are associated with molecularly proximate moieties. For example, **Figure 3**A shows a 2D $^{13}C\{^1H\}$ HETCOR spectrum acquired for a PBTTT-C16:$PC_{71}BM$ blend with a molar ratio of 1:1. This spectrum exhibits strong 2D intensity correlations (red, blue arrows) between ^{13}C and ^1H signals from the conjugated polymer (orange) and the fullerene derivative (blue) that establish their mutual molecular proximities (<1 nm). Such

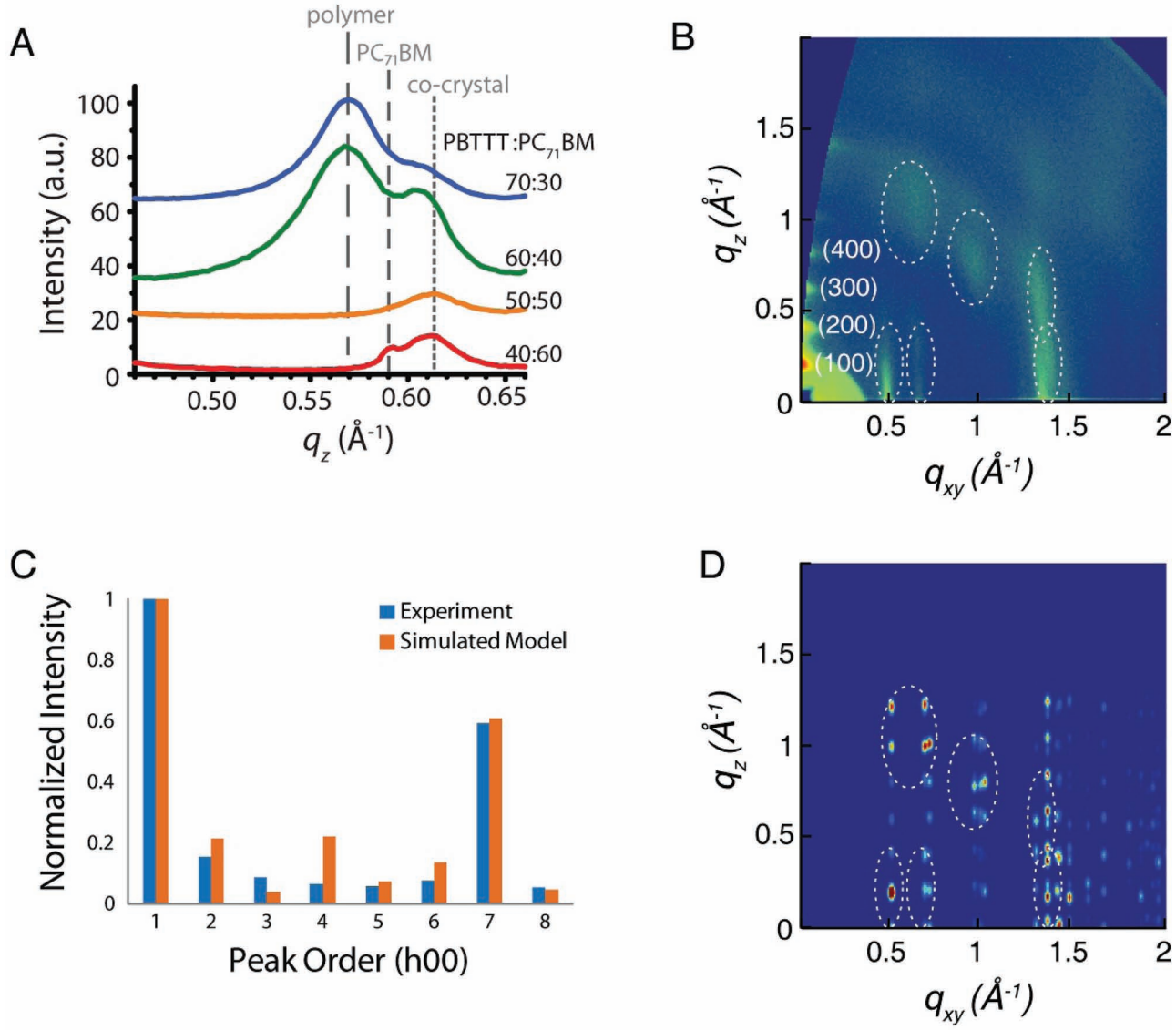

Figure 2. A) Specular XRD patterns for PBTTT-C14:$PC_{71}BM$ blends with a range of molar ratios. B) Experimental 2D GIXS pattern for the bimolecular crystal. The highest-intensity non-specular reflections are circled for comparison to the simulated pattern in (D). C) Specular XRD reflection intensities normalized by the (*100*) peak intensity. The experimental data are shown in blue, and the intensities calculated from the structure factor of the simulated unit cell are shown in orange. D) Calculated 2D GIXS pattern for the simulated unit cell. A list of the diffraction peak positions is given in Table S2 in the Supporting Information.

intensity correlations provide unambiguous proof of the intercalation of the fullerene derivative in the polymer network.

Specifically, signals associated with ^{13}C moieties from the $PC_{71}BM$ side group (e.g., at 172 ppm from the C=O groups, at 129 ppm from the phenyl rings, and at 36 and 73 ppm from the cyclopropane anchor) are correlated with ^{1}H signals at 1.4 ppm from the aliphatic PBTTT-C16 polymer side chains. Additional intensity correlations are observed between ^{13}C signals from the C_{70} fullerene moieties and ^{1}H signals at 1.4, 7.2, and 8.7 ppm from the aliphatic side chains and the aromatic backbone protons of PBTTT-C16, respectively. These correlated 2D NMR spectroscopy signal intensities establish strong interactions and hence close molecular proximities between these molecular moieties. Furthermore, separate solid-state $^{1}H\{^{1}H\}$ double-quantum NMR spectroscopy analyses enabled the local distances between different aromatic proton moieties to be determined (Supporting Information, Table S3). Specifically, the ^{1}H signals at 7.2 and 8.7 ppm correspond to distinct thienothiophene moieties and provide important quantitative constraints that allow the structure of the bimolecular crystal to be confidently established. A detailed discussion of these analyses are beyond the scope of this paper and will be published in the near future.

Considering the XRD and NMR spectroscopy results, a monoclinic unit cell with one PBTTT-C14 monomer per fullerene molecule, straight side chains, and planar polymer backbones is a plausible starting point for MM modeling of the structure. To fine tune the atomic positions, the unit-cell parameters and

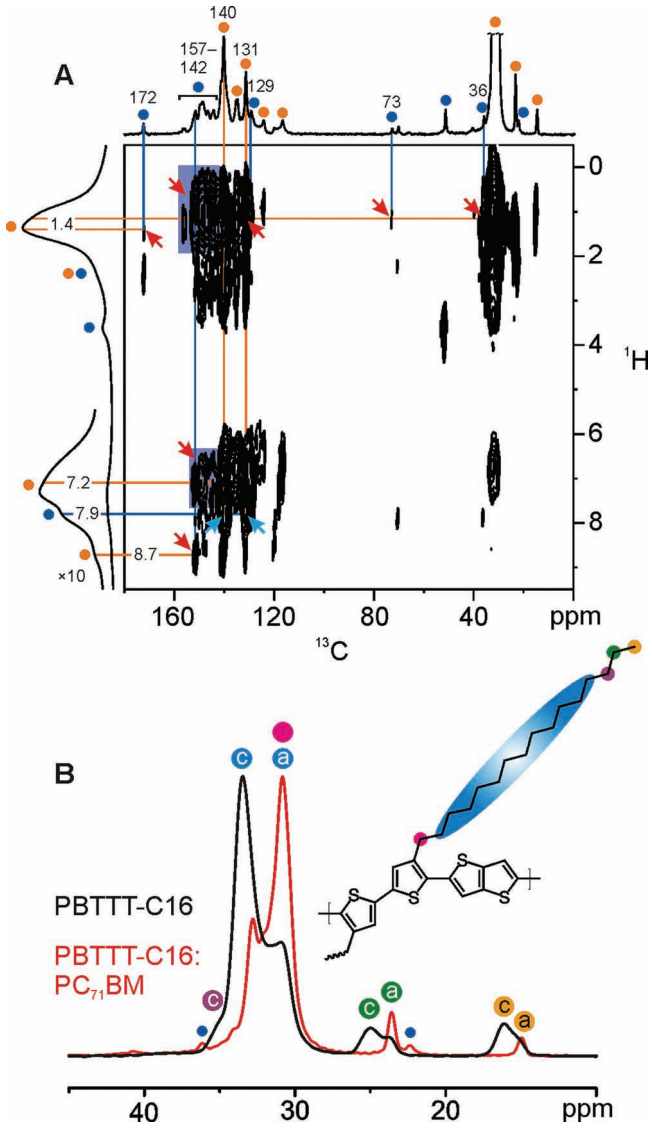

Figure 3. A) 2D $^{13}C\{^1H\}$ HETCOR NMR spectrum of a PBTTT-C16:$PC_{71}BM$ blend with a molar ratio of 1:1. A corresponding 1D $^{13}C\{^1H\}$ CP/MAS spectrum is shown along the top horizontal axis, and a 1D single-pulse ^1H MAS spectrum is shown along the left vertical axis. The orange and blue circles indicate spectral contributions from the PBTTT-C16 and the $PC_{71}BM$, respectively. Lines are shown to aid the identification of correlated signal intensities that establish spatial proximities between specific moieties of the conjugated polymer and the fullerene derivative. The red arrows mark correlated signals between the ^{13}C moieties of the $PC_{71}BM$ and the ^1H moieties of the PBTTT-C16, consistent with the proposed crystal structure. The light-blue arrows mark correlated signals between the aromatic ^{13}C moieties of the conjugated polymer and the protons from the $PC_{71}BM$ side-chain, revealing local structural disorder of fullerene orientations in the polymer crystal. B) Aliphatic regions of 1D $^{13}C\{^1H\}$CP/MAS spectra of the PBTTT-C16:$PC_{71}BM$ blend (red) and the neat polymer (black) recorded under MAS conditions of 12.5 kHz with a CP contact time of 2 ms. The colored circles assign the ^{13}C moieties of the PBTTT-C16 side chains in the crystalline (c) and amorphous (a) regions to their respective signals in the 2D spectrum.

atomic positions were relaxed to minimize the energy associated with intermolecular interactions. The simulations were conducted iteratively until there was good agreement of the measured

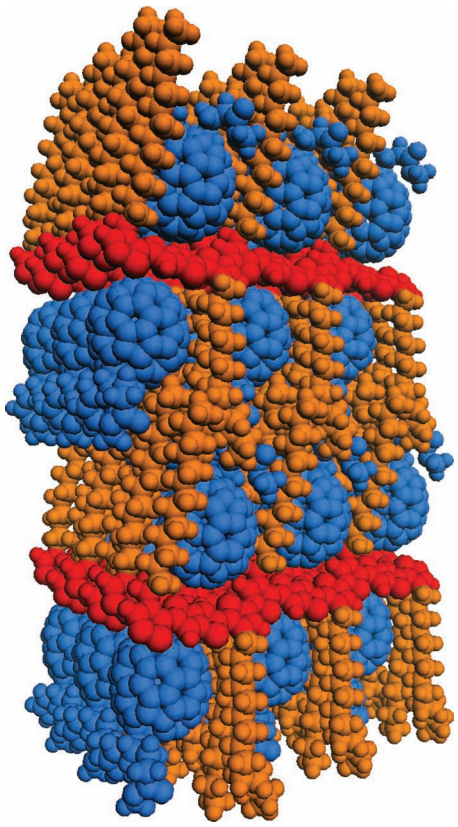

Figure 4. An extended space-filling structure of the PBTTT-C14:$PC_{71}BM$ bimolecular crystal based on the simulated unit cell. The polymer backbones, polymer side chains and fullerene molecules are red, orange and blue, respectively.

XRD patterns and the local proton distances determined by ^1H NMR spectroscopy (Supporting Information, Table S3) with those calculated for the minimum-energy structure. The resulting structure, which is shown in **Figure 4** (and is provided in cif format in the Supporting Information), has twisted and bent polymer backbones, bent side chains, and is triclinic with the angles β and γ both equal to 89° (e.g., close to the 90° initial guess). A 1 ns molecular dynamics (MD) simulation for a $2 \times 3 \times 2$ super cell at room temperature showed stabilization both in energy and density after a short period of time (200 ps). Both the MM energy-minimized structure and one acquired from a snapshot of the $2 \times 3 \times 2$ super cell obtained towards the end of the MD simulation correlate well with each other in terms of their correspondence with the proton-proton distances determined by the 2D NMR spectroscopy measurements and in their use to simulate the 2D GIXS pattern (Supporting Information, Figure S4).

The experimental and calculated specular XRD intensities are compared in Figure 2C. These reflection intensities are sensitive to the electron density perpendicular to the substrate. The $PC_{71}BM$ position and orientation, the polymer-backbone tilt angle, and the $PC_{71}BM$ mole fraction primarily determine the electron density in the normal direction. The experimental intensities were corrected for the Lorentz factor, the change in irradiated volume with q, the polarization, and the Debye–Waller

factor to allow comparison with intensities calculated from the simulated unit cell. The good agreement between the experimental intensities (blue) and the calculated intensities for the simulated unit cell (orange) supports the accuracy of the simulated unit cell. In particular, the model captures the unexpectedly intense (*700*) reflection.

Comparison of the experimental 2D GIXS pattern (Figure 2B) with the calculated pattern for the simulated unit cell (Figure 2D) shows good agreement of the reflection positions. Nevertheless, the experimental GIXS pattern exhibits several reflections that are broader, compared to the calculated pattern, which are attributed to defects (i.e., lamellar stacking disruptions) and disorder within the bimolecular crystal that are not captured in the modeling. The MM simulations revealed several similar structures with comparable total energies. Such a flat energy landscape allows geometric fluctuations within the bimolecular crystal, which can account for the broadening of the scattering reflections.

The solid-state NMR spectroscopy results also confirm disorder in the polymer side chains and the fullerene orientation. For instance, the light blue arrows in the 2D $^{13}C\{^1H\}$ HETCOR spectrum shown in Figure 3A mark the correlated intensity between the ^{13}C signals at 131, 135, and 140 ppm from the aromatic moieties of the conjugated polymer backbone and the ^1H signals at 7.9 ppm from the phenyl moieties of the $PC_{71}BM$ side group. Such interactions can only be realized with a different orientation of $PC_{71}BM$ in the polymer crystal, reflecting a distribution of local configurations that are not apparent in the structure shown in Figure 4 and **Figure 5**. In this case, the $PC_{71}BM$ moiety must be flipped by 180°, such that the $PC_{71}BM$ side group points toward the PBTTT-C16 backbone. Thus, NMR spectroscopy provides direct proof of local structural disorder regarding the fullerene orientation, in line with the observed flat energy landscape in MM simulations and broadening of the XRD reflections. Such orientational disorder may cause disruptions of the 1D fullerene channels and decrease the efficiency of electron transport via these pathways.

Additionally, the insertion of $PC_{71}BM$ into the PBTTT-C16 crystal results in local disorder of the alkyl side chains. Figure 3B shows the aliphatic regions of 1D $^{13}C\{^1H\}$ CP/MAS NMR spectra of neat PBTTT-C16 and its 1:1 blend with $PC_{71}BM$. Colored circles assign the signals to their respective structural moieties. For the neat polymer, each moiety gives rise to two spectral contributions with slightly different ^{13}C isotropic chemical shifts; the high-frequency contributions arise from ^{13}C moieties with γ-neighbors in all-*trans* conformations, a necessary prerequisite for crystalline regions, and the low-frequency contributions are due to *gauche* conformations, which are less ordered and not present in crystalline domains.[22,23] For neat PBTTT-C16, the main fraction of the ^{13}C signals stems from well-ordered, crystalline side chains, although there is some intensity from disordered side chains, which manifests the presence of a significant fraction of disordered PBTTT-C16 side chains. Upon intercalation of $PC_{71}BM$, almost all of the aliphatic ^{13}C signal intensity in the PBTTT-C16:$PC_{71}BM$ blend arises from such disordered side chains. Disorder in the PBTTT-C14 side chains in the bimolecular crystal was also verified by observing Fourier transform IR (FTIR) spectroscopy spectral shifts in the anti-symmetric stretching frequencies of the methylene units in the alkyl chains in PBTTT-C14:$PC_{71}BM$ blends as a function of composition (Supporting Information, Table S5). Thus, the good agreement between the calculated and experimental specular XRD intensities and 2D GIXS patterns suggests that the structure of the bimolecular crystal closely resembles that of the simulated unit cell, while the 2D NMR spectroscopy intensity correlations and infrared spectroscopy show some variation in the fullerene orientation and side-chain conformations throughout the crystal.

Expanded structures based on the simulated bimolecular-crystal unit cell are shown in Figure 4,5 with the polymer backbones, polymer side chains, and fullerene molecules shown in red, orange, and blue, respectively. An enlarged version of Figure 5D with a stereoscopic image for viewing with red/blue 3D glasses is shown in Figure S9 in the Supporting Information. These figures emphasize important features of the bimolecular crystal and the significant differences between the molecular packing in pure PBTTT-C14[24,25] and the PBTTT-C14:$PC_{71}BM$ bimolecular crystal. Such features are similar to those observed for films using PBTTT with $-C_{12}H_{25}$ and $-C_{16}H_{33}$ side chains, which exhibit similar XRD patterns (Supporting Information, Figure S5, S6). The most-obvious differences between the structures are the increase in the spacing of the (*100*) planes due to fullerene insertion (Figure 5A,D) and the formation of fullerene channels that only support 1D electron transport; the PBTTT-C14 side chains and backbones interfere with electron transport in the other directions (Figure 4,5E). In addition, the side chains, which tilt at an angle of ≈35° in the neat PBTTT-C14 polymer (Figure 5A), bend in the bimolecular crystal to allow dense packing in the interdigitated regions, while maintaining enough space for fullerene intercalation near the PBTTT-C14 backbone (Figure 5D). Further evidence for the side-chain conformations shown in Figure 5A,D was obtained by confirming that the lamellar spacings from XRD patterns of pure PBTTT and PBTTT:$PC_{71}BM$ blends with $-C_{12}H_{25}$, $-C_{14}H_{29}$, and $-C_{16}H_{33}$ side chains match those predicted by the modeling (Supporting Information, Figure S5). Likewise, the backbone stagger along the *c*-axis changes to accommodate the intercalated fullerene in the bimolecular crystal (Figure 5C,F).

Fullerene intercalation also substantially changes the stacking of the PBTTT-C14 backbones, as depicted in Figure 5B,E. The positions of the polymer backbones alternate up and down, as half of the backbones interact with the fullerenes in the upper part of the unit cell, while the other half interact with fullerenes in the lower part of the unit cell (Figure 5E). Moreover, the thienothiophene units closest to the fullerene molecules twist with respect to the rest of the polymer backbone, presumably to improve the intermolecular interactions between the PBTTT-C14 backbone and the fullerenes. The 3D renderings of the structures (Supporting Information, Figure S9) show that the backbones also bend slightly and wrap around the fullerenes. This twisting and bending results in a non-planar polymer backbone with twist angles between the thienothiophene and thiophene moieties ranging from 10° to 40°.

These molecular packing features explain important properties of PBTTT-C14:$PC_{71}BM$ blends. For instance, the backbone twists and backbone-fullerene interactions explain why the PBTTT-C14:$PC_{71}BM$ absorption spectrum differs significantly from the superposition of the PBTTT-C14 and $PC_{71}BM$

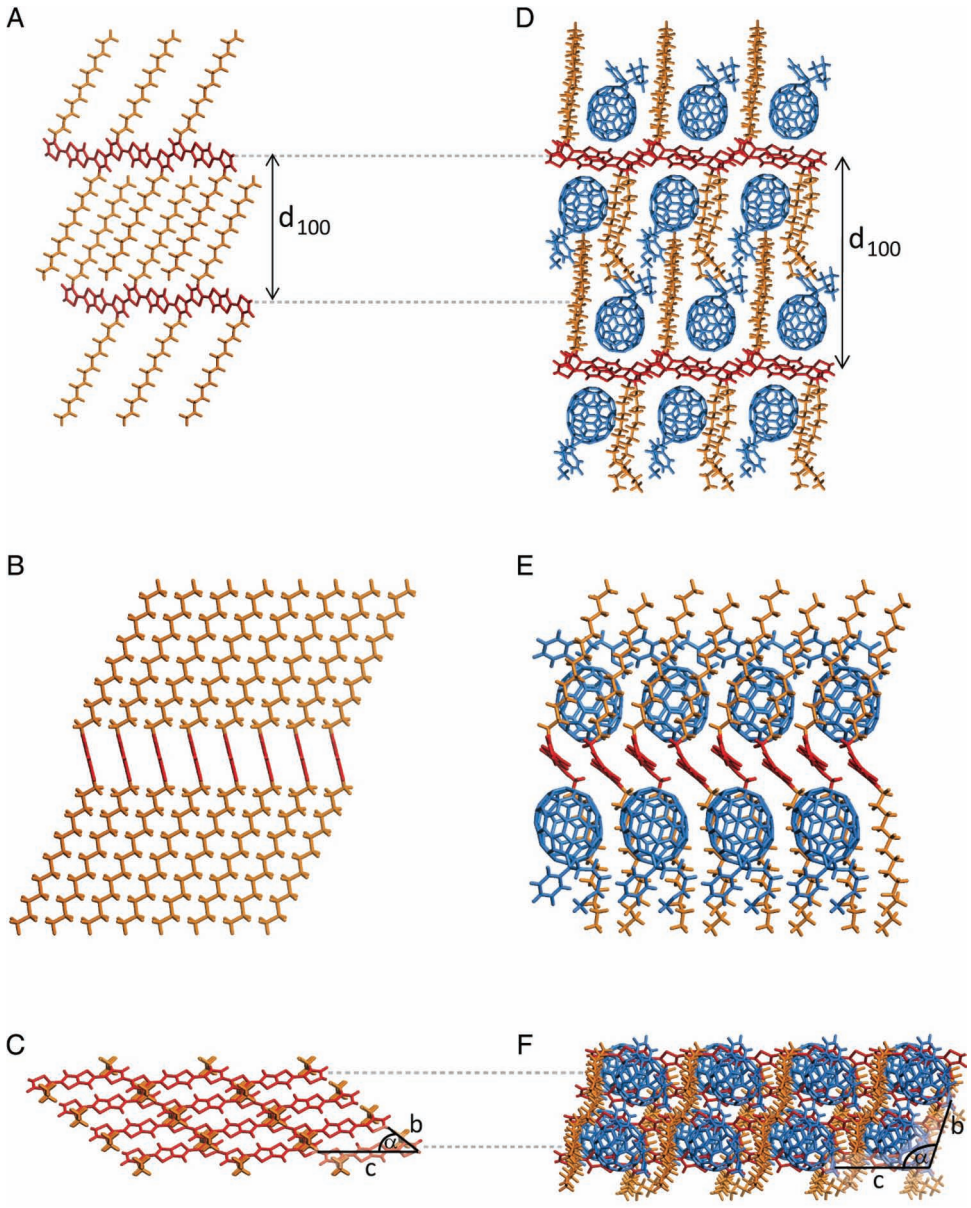

Figure 5. Molecular structures of the pure PBTTT-C14 (A–C) and the PBTTT-C14:$PC_{71}BM$ (D–E) bimolecular crystal viewed along the *b*-axis (A,D) the *c*-axis (B,E), and the side chains (C,F). The polymer backbones, polymer side chains and fullerenes are red, orange and blue, respectively. The projection of the *b* and *c* axes and the angle α are shown in (C) and (F). Note that these structures do not capture the disorder present in the films, since every unit cell in these structures is the same. Warren–Averbach analysis of the specular diffraction peaks gives an out-of-plane crystallite size and paracrystallinity parameter of ≈24 nm and ≈2%, respectively.[45,46] Thus, the actual structure of the films will contain more disorder than is apparent in these figures.

absorption spectra.[17,26] Likewise, the previously observed order-of-magnitude decrease in the PBTTT-C14 hole mobility upon the addition of $PC_{71}BM$ can be attributed not only to the dilution of the hole-transporting material, but also to the disruption of the polymer π-stacking that results both from the backbone twists and the additional unit-cell volume required to account for the intercalated fullerene.[10,27] Indeed, density functional theory (DFT) calculations (Supporting Information, Table S4) reveal that the electronic coupling between polymer chains along the backbone-stacking direction (*b*-axis) drops by an order-of-magnitude in the presence of intercalated $PC_{71}BM$.

In addition, DFT calculations indicate that there is non-negligible electronic coupling (≈20–40 meV) for electrons between neighboring $PC_{71}BM$ molecules along the *b*-axis in the bimolecular crystal, but negligible electronic coupling strength (≈0 meV) between $PC_{71}BM$ along other directions. This implies a possible electron-transport pathway through the 1D $PC_{71}BM$ channels. The very low electron mobility in bimolecular-crystal films can be attributed to the 1D character of the fullerene channels and the disorder of the fullerenes in the bimolecular crystal.[10] In a polycrystalline film, it is expected to be difficult for electrons to move between differently oriented crystals,

because the 1D electron channels will not generally be aligned. Moreover, electron transport perpendicular to the substrate, which is critical for solar cell operation, will be especially difficult, because the PBTTT-C14:$PC_{71}BM$ bimolecular crystals generally form lamellar structures with the electron channels running parallel, rather than perpendicular, to the substrate. The low electron mobility does not appear to be a result of a large fullerene-fullerene distance in the bimolecular crystal, because the average fullerene separation in the simulated unit cell is 9.8 Å, which is comparable to the reported center-to-center distance of 9.88 Å in a C_{70} crystal.[28] On-going quantum-chemical calculations, based on the optimized structures, should prove useful to understand the electronic properties of the bimolecular crystals at a deeper level.

Since fullerenes intercalate between the side chains of many polymers used in solar cells, PBTTT:$PC_{71}BM$ is a valuable model system. While it will not be possible to use XRD to determine the structure of other polymer-fullerene mixed phases in cases where there are only a few XRD peaks, it should be possible to generate approximate structures by assuming that fullerenes alter the polymer packing in ways that are similar to those reported in this study. Molecular mechanics and molecular dynamics simulations can be used to fine tune these structures to be consistent with constraints provided by NMR and FTIR spectroscopy. Now that the structure of the important PBTTT-C14:$PC_{71}BM$ model system is known, it will be fruitful to compare theoretical property predictions based on the structure with measurements made by powerful spectroscopic techniques, such as UV–vis, NMR, and Raman spectroscopy. When the accuracies and agreement of the theoretical and spectroscopy tools are validated, it will be possible to use them with less ordered materials to gain information that has not been previously obtainable. We expect that solid-state NMR spectroscopy, which has been rarely used to investigate bulk heterojunctions,[21,29–31] will be provide helpful insights for determining how fullerenes interact with the complex donor-acceptor polymers that enable the highest power conversion efficiencies. Knowing more about how molecules pack in bulk heterojunctions will be useful to researchers trying to understand why recombination is much slower in some polymer-fullerene blends than others and will enable the design of more efficient solar cells. More generally, the complicated interplay of molecular order and disorder in the polymer:fullerene bimolecular crystal is intrinsic to numerous other semicrystalline materials, especially those for which molecular interactions at surfaces broadly govern macroscopic properties. These include diverse semicrystalline polymers or hybrid nanocomposites that are used broadly as ion-conducting membranes in fuel cells or batteries,[32] as environmental barriers or for structural packaging in microelectronics,[33] or as dye hosts in opto-electronic applications.[34] For these and related systems, feedback among complementary synthesis, characterization, and modeling strategies are key to improving material properties to reach device and technology performance targets.

Experimental Section

Materials: PBTTT was synthesized with $-C_{12}H_{25}$, $-C_{14}H_{29}$ and $-C_{16}H_{33}$ side chains as described by McCulloch et al.[27] The number-average molecular masses (M_n) of PBTTT with $-C_{12}H_{25}$, $-C_{14}H_{29}$ and $-C_{16}H_{33}$ side chains were determined to be 28, 22, and 35 kDa with polydispersities of 1.8, 2.0, and 2.0, respectively, using gel-permeation chromatography (GPC) against polystyrene standards. $PC_{71}BM$ was purchased from NanoC. The PBTTT:$PC_{71}BM$ films for X-ray diffraction were spin-cast from *ortho*-dichlorobenzene on octadecyltrichlorosilane (OTS)-coated silicon substrates and annealed at 180 °C for 10 min. For the NMR spectroscopy measurements, PBTTT-C16:$PC_{71}BM$ films with a molar ratio of 1:1 were drop-cast from *ortho*-dichlorobenzene on octadecyltrichlorosilane (OTS)-coated silicon substrates and annealed at 180 °C for 10 min. The structural similarity of drop-cast and spin-cast films was confirmed by XRD.

X-Ray Diffraction: 2D GIXS measurements were performed at the Stanford Synchrotron Radiation Laboratory (SSRL) on beamline 11-3 at an energy of 12.7 keV and an incidence angle of 0.10° using a MAR345 image plate area detector. We omitted the features near $q_{xy} = 0$ from our experimental 2D GIXS data, as these peaks are not accurately measured in image plate collection geometry.[35] High-resolution specular diffraction and high-resolution grazing-incidence X-ray diffraction were performed at an energy of 8 keV on SSRL beamlines 2-1 and 7-2, respectively. To produce PBTTT-C14:$PC_{71}BM$ films with a preferred in-plane orientation, we aligned pure PBTTT-C14 using a flow-coating method[18] and subsequently spin-cast a $PC_{71}BM$ layer on top of the aligned PBTTT-C14 film by using the orthogonal solvent dichloromethane (DCM). Annealing allowed diffusion between the layers and resulted in the coexistence of aligned PBTTT-C14, aligned bimolecular crystals and randomly-oriented $PC_{71}BM$ as shown in the specular X-ray diffraction data (Supporting Information, Figure S1).

IR Spectroscopy: IR spectroscopy was performed using a commercial FTIR spectrometer. The samples were mounted on a custom transmission stage such that the IR beam was incident on the samples nominally at Brewster's angle (about 72°). The polarization of the IR beam was controlled by a wire-grid polarizer placed immediately before the sample stage. The IR spectroscopy results were fitted with a least-squares regression of both *s*- and *p*-polarized spectra simultaneously.

Theoretical Modeling: Molecular mechanics (MM) and molecular dynamics (MD) simulations were performed on the PBTTT-C14:$PC_{71}BM$ unit cell using the universal force field, as described by Rappe et al.,[36] as employed in the Materials Studio software suite. The SimDiffraction code[37] was used to simulate the XRD patterns of the optimized blend unit cells. The a^* direction of the crystal unit cell was set to be oriented parallel to the substrate normal. The diffraction simulation conditions were set to be identical to the experiment. The in-plane and out-of-plane orientations were set as infinity and 10°, respectively, to describe the preferential orientation distribution of the films. The intensity of the diffracted peaks was calculated by accounting for the Lorentz factor, the polarization factor, and the Debye-Waller factor, as described in the literature.[37] Density functional theory calculations were carried out at the B3LYP/6-31G** level. The evaluation of the nearest-neighbor effective transfer integral (electronic coupling) was determined through the use of a fragment orbital approach in combination with a basis set orthogonalization procedure.[38]

Solid-State NMR Spectroscopy: Solid-state NMR spectra were recorded on a Bruker AVANCE II NMR spectrometer with an 11.7 Tesla wide-bore superconducting magnet, operating at Larmor frequencies of 500.24 MHz for ^1H and 125.79 MHz for ^{13}C. The experiments were conducted at 293 K on films that were scraped off substrates and loaded into 4.0 mm zirconia rotors with Kel-F caps and measured using a 4.0 mm double-resonance H-X magic-angle-spinning (MAS) probehead under MAS conditions at a rotation rate of 12.5 kHz. The spectra were acquired with a ^1H 90°-pulse length of 2.5 µs, corresponding to a radio frequency (rf)-field strength of 100 kHz, and a relaxation delay of 1.5 s. For the 1D ^{13}C cross-polarization (CP)/MAS and 2D $^{13}C\{^1H\}$ HETCOR spectra, magnetization was transferred from ^1H to ^{13}C nuclei through CP by adiabatic passage with a contact time of 2 ms.[39] A broadband SPINAL-64 heteronuclear ^1H decoupling scheme was used during detection.[40] For the 2D $^{13}C\{^1H\}$ HETCOR spectrum, quadrature

detection in the indirect ^{1}H dimension was achieved by using the States-TPPI detection scheme.[41] Homonuclear dipolar couplings affecting the ^{1}H dimension were reduced by applying high power ^{1}H–^{1}H homonuclear decoupling using the eDUMBO-1_{22} sequence during the proton spin evolution time t_1 with a phase-modulated rf pulse of constant amplitude (100 kHz).[42] 80 t_1 increments of 128 µs with 848 transients per increments were recorded. In the indirect ^{1}H dimension, a scaling factor of 0.601 was determined experimentally with a 2D ^{1}H{^{1}H} homonuclear correlation experiment. The chemical shifts are reported relative to tetramethylsilane (TMS) using tetrakis(trimethylsilyl) silane (TKS) and adamantane as secondary standards for ^{1}H and ^{13}C, respectively.[43,44]

Supporting Information

Supporting Information is available from the Wiley Online Library or from the author.

Acknowledgements

This work was supported by the Center for Advanced Molecular Photovoltaics (Award No KUS-C1-015-21), made by King Abdullah University of Science and Technology (KAUST). We thank Madhusudhanan Srinivasan and Dina Garatly (KAUST Visualization Center) for help in visualizing the three-dimensional structures and preparing the figures, and Craig Kapfer (KAUST IT), and Dodi Heryadi (KAUST Supercomputing Lab and Noor cluster) for assistance with the molecular-dynamics simulations. We would also like to thank Jonathan Rivnay for performing Warren-Averbach analyses on our materials. The work at UCSB was supported in part by the USARO through the Institute for Collaborative Biotechnologies under contract no. W911NF-09-D-0001. The NMR spectroscopy experiments were conducted in the Central Facilities of the UCSB Materials Research Laboratory supported by the MRSEC program of the US NSF under award no. DMR-0520415. R.G. and N.C.M were supported by a Swiss National Science Foundation and an NSF Fellowship, respectively. M.J.N.J. acknowledges financial support from the Alexander von Humboldt-Foundation through a Feodor Lynen Research Fellowship. Portions of this research were carried out at the Stanford Synchrotron Radiation Lightsource, a national user facility operated by Stanford University on behalf of the US Department of Energy, Office of Basic Energy Sciences. We acknowledge the permission to use the *Wxdiff* diffraction-image-processing and data-analysis software package by Stefan C. B. Mannsfeld at SSRL (http://code.google.com/p/wxdiff) and important insight on the simulation of X-ray diffraction patterns from conversations with Dag W. Breiby. The authors thank Eric Verploegen for assistance with the He-flow sample chamber at SSRL. Certain commercial equipment, instruments, or materials are identified in this paper to specify the experimental procedures adequately. Such identification is not intended to imply recommendation or endorsement by the National Institute of Standards and Technology, nor is it intended to imply that the materials or equipment identified are necessarily the best available for the purpose.

Received: June 7, 2012
Revised: August 9, 2012
Published online: September 5, 2012

[1] G. Yu, J. Gao, J. C. Hummelen, F. Wudl, A. J. Heeger, *Science* **1995**, *270*, 1789.
[2] Z. He, C. Zhong, X. Huang, W.-Y. Wong, H. Wu, L. Chen, S. Su, Y. Cao, *Adv. Mater.* **2011**, *23*, 4636.
[3] B. C. Thompson, J. M. J. Fréchet, *Angew. Chem. Int. Ed.* **2008**, *47*, 58.
[4] *Press Release*, *Solarmer Energy, Inc.,* **July 27, 2010**.
[5] *Press Release*, *Konarka,* **November 29, 2010**.
[6] E. H. Yonemoto, G. B. Saupe, R. H. Schmehl, S. M. Hubig, R. L. Riley, B. L. Iverson, T. E. Mallouk, *J. Am. Chem. Soc.* **1994**, *116*, 4786.
[7] J. L. Brédas, J. P. Calbert, D. A. da Silva, J. Cornil, *Proc. Natl. Acad. Sci. USA* **2002**, *99*, 5804.
[8] M. Mas-Torrent, P. Hadley, S. T. Bromley, X. Ribas, J. Tarrés, M. Mas, E. Molins, J. Veciana, C. Rovira, *J. Am. Chem. Soc.* **2004**, *126*, 8546.
[9] Y. Kanai, J. C. Grossman, *Nano Lett.* **2007**, *7*, 1967.
[10] A. C. Mayer, M. F. Toney, S. R. Scully, J. Rivnay, C. J. Brabec, M. Scharber, M. Koppe, M. Heeney, I. McCulloch, M. D. McGehee, *Adv. Funct. Mater.* **2009**, *19*, 1173.
[11] N. D. Treat, M. A. Brady, G. Smith, M. F. Toney, E. J. Kramer, C. J. Hawker, M. L. Chabinyc, *Adv. Energy Mater.* **2011**, *1*, 82.
[12] D. Chen, F. Liu, C. Wang, A. Nakahara, T. P. Russell, *Nano Lett.* **2011**, *11*, 2071.
[13] B. A. Collins, E. Gann, L. Guignard, X. He, C. R. McNeill, H. Ade, *J. Phys. Chem. Lett.* **2010**, *1*, 3160.
[14] W. Yin, M. Dadmun, *ACS Nano* **2011**, *5*, 4756.
[15] N. C. Miller, R. Gysel, C. E. Miller, E. Verploegen, Z. Beiley, M. Heeney, I. McCulloch, Z. Bao, M. F. Toney, M. D. McGehee, *J. Polym. Sci., Part B: Polym. Phys.* **2011**, *49*, 499.
[16] J. E. Parmer, A. C. Mayer, B. E. Hardin, S. R. Scully, M. D. McGehee, M. Heeney, I. McCulloch, *Appl. Phys. Lett.* **2008**, *92*, 113309.
[17] N. C. Cates, R. Gysel, Z. Beiley, C. E. Miller, M. F. Toney, M. Heeney, I. McCulloch, M. D. McGehee, *Nano Lett.* **2009**, *9*, 4153.
[18] D. M. DeLongchamp, R. J. Kline, Y. Jung, D. S. Germack, E. K. Lin, A. J. Moad, L. J. Richter, M. F. Toney, M. Heeney, I. McCulloch, *ACS Nano* **2009**, *3*, 780.
[19] H. W. Spiess, *Macromolecules 43*, 5479.
[20] K. Schmidt-Rohr, H. W. Spiess, *Multidimensional Solid-State NMR and Polymers*, Academic Press, London **1994**.
[21] C. Yang, J. G. Hu, A. J. Heeger, *J. Am. Chem. Soc.* **2006**, *128*, 12007.
[22] F. A. Bovey, L. W. Jelinski, *Chain Structure and Conformation of Macromolecules*, Academic Press, New York **1982**.
[23] S. Neyshtadt, J. P. Jahnke, R. J. Messinger, A. Rawal, T. Segal Peretz, D. Huppert, B. F. Chmelka, G. L. Frey, *J. Am. Chem. Soc.* **2011**, *133*, 10119.
[24] P. Brocorens, A. Van Vooren, M. L. Chabinyc, M. F. Toney, M. Shkunov, M. Heeney, I. McCulloch, J. Cornil, R. Lazzaroni, *Adv. Mater.* **2009**, *21*, 1193.
[25] E. Cho, C. Risko, D. Kim, R. Gysel, N. C. Miller, D. W. Breiby, M. D. McGehee, M. F. Toney, R. J. Kline, J.-L. Brédas, *J. Am. Chem. Soc.* **2012**, *134*, 6177.
[26] I.-W. Hwang, J. Young Kim, S. Cho, J. Yuen, N. Coates, K. Lee, M. Heeney, I. McCulloch, D. Moses, A. J. Heeger, *J. Phys. Chem. C* **2008**, *112*, 7853.
[27] I. McCulloch, M. Heeney, C. Bailey, K. Genevicius, I. Macdonald, M. Shkunov, D. Sparrowe, S. Tierney, R. Wagner, W. M. Zhang, M. L. Chabinyc, R. J. Kline, M. D. McGehee, M. F. Toney, *Nat. Mater.* **2006**, *5*, 328.
[28] E. Blanc, H.-B. Bürgi, R. Restori, D. Schwarzenbach, P. Stellberg, P. Venugopalanc, *Europhys. Lett.* **1994**, *27*, 359.
[29] R. C. Nieuwendaal, C. R. Snyder, R. J. Kline, E. K. Lin, D. L. VanderHart, D. M. DeLongchamp, *Chem. Mater.* **2010**, *22*, 2930.
[30] R. Mens, S. Chambon, S. Bertho, G. Reggers, B. Ruttens, J. D'Haen, J. Manca, R. Carleer, D. Vanderzande, P. Adriaensens, *Magn. Reson. Chem.* **2011**, *49*, 242.
[31] H. Kaji, H. Hayashi, T. Yamada, M. Fukuchi, S. Fujimura, M. Ueda, S. Kang, T. Umeyama, Y. Matano, H. Imahori, *Appl. Phys. Lett.* **2011**, *98*, 113301.

[32] M. A. Hickner, H. Ghassemi, Y. S. Kim, B. R. Einsla, J. E. McGrath, *Chem. Rev.* **2004**, *104*, 4587.
[33] J. Lange, Y. Wyser, *Packag. Technol. Sci.* **2003**, *16*, 149.
[34] J. Kido, H. Shionoya, K. Nagai, *Appl. Phys. Lett.* **1995**, *67*, 2281.
[35] M. L. Chabinyc, *Polym. Rev.* **2008**, *48*, 463.
[36] A. K. Rappe, C. J. Casewit, K. S. Colwell, W. A. Goddard, W. M. Skiff, *J. Am. Chem. Soc.* **1992**, *114*, 10024.
[37] D. W. Breiby, O. Bunk, J. W. Andreasen, H. T. Lemke, M. M. Nielsen, *J. Appl. Crystallogr.* **2008**, *41*, 262.
[38] E. F. Valeev, V. Coropceanu, D. A. da Silva Filho, S. Salman, J.-L. Brédas, *J. Am. Chem. Soc.* **2006**, *128*, 9882.
[39] S. Hediger, B. H. Meier, N. D. Kurur, G. Bodenhausen, R. R. Ernst, *Chem. Phys. Lett.* **1994**, *223*, 283.
[40] B. M. Fung, A. K. Khitrin, K. Ermolaev, *J. Magn. Reson.* **2000**, *142*, 97.
[41] D. Marion, M. Ikura, R. Tschundin, A. Bax, *J. Magn. Reson.* **1989**, *85*, 393.
[42] B. Elena, G. de Paëpe, L. Emsley, *Chem. Phys. Lett.* **2004**, *398*, 532.
[43] J. V. Muntean, L. M. Stock, R. E. Botto, *Energy Fuels* **1988**, *2*, 108.
[44] C. R. Morcombe, K. W. Zilm, *J. Magn. Reson.* **2003**, *162*, 479.
[45] J. Rivnay, R. Noriega, R. J. Kline, A. Salleo, M. F. Toney, *Phys. Rev. B: Condens. Matter* **2011**, *84*, 045203.
[46] S. U. Jonathan Rivnay, *Personal Communication*, **2012**.